

Article

Ground Ammonia Concentrations over China Derived from Satellite and Atmospheric Transport Modeling

Lei Liu ¹, Xiuying Zhang ^{1,*}, Wen Xu ², Xuejun Liu ², Xuehe Lu ¹, Shanqian Wang ¹, Wuting Zhang ¹ and Limin Zhao ^{1,3}

¹ Jiangsu Provincial Key Laboratory of Geographic Information Science and Technology, International Institute for Earth System Science, Nanjing University, Nanjing 210023, China; liulei_nju_geo@163.com (L.L.); luxh43@gmail.com (X.L.); shanqianwang@163.com (S.W.); zhangwuting75@163.com (W.Z.); zlm2016nju@163.com (L.Z.)

² College of Resources and Environmental Sciences, Centre for Resources, Environment and Food Security, Key Lab of Plant-Soil Interactions of MOE, China Agricultural University, Beijing 100193, China; hi.xuwen@163.com (W.X.); liu310@cau.edu.cn (X.L.)

³ Jiangsu Center for Collaborative Innovation in Geographical Information Resource Development and Application, Nanjing 210023, China

* Correspondence: lzhxy77@163.com

Academic Editors: Yang Liu, Jun Wang, Omar Torres, Richard Müller and Prasad S. Thenkabail

Received: 27 March 2017; Accepted: 7 May 2017; Published: 15 May 2017

Abstract: As a primary basic gas in the atmosphere, atmospheric ammonia (NH₃) plays an important role in determining air quality, environmental degradation, and climate change. However, the limited ground observation currently presents a barrier to estimating ground NH₃ concentrations on a regional scale, thus preventing a full understanding of the atmospheric processes in which this trace gas is involved. This study estimated the ground NH₃ concentrations over China, combining the Infrared Atmospheric Sounding Interferometer (IASI) satellite NH₃ columns and NH₃ profiles from an atmospheric chemistry transport model (CTM). The estimated ground NH₃ concentrations showed agreement with the variability in annual ground NH₃ measurements from the Chinese Nationwide Nitrogen Deposition Monitoring Network (NNDMN). Great spatial heterogeneity of ground NH₃ concentrations was found across China, and high ground NH₃ concentrations were found in Northern China, Southeastern China, and some areas in Xinjiang Province. The maximum ground NH₃ concentrations over China occurred in summer, followed by spring, autumn, and winter seasons, which were in agreement with the seasonal patterns of NH₃ emissions in China. This study suggested that a combination of NH₃ profiles from CTMs and NH₃ columns from satellite obtained reliable ground NH₃ concentrations over China.

Keywords: NH₃; satellite; CTM; spatial; ground

1. Introduction

Ammonia (NH₃) is the primary form of reactive nitrogen (Nr) in the environment and a key component of the ecosystems, representing more than half of atmospheric Nr emissions [1,2]. NH₃ emissions have been increasing in recent years due to the increasing agricultural livestock numbers and the increasing application of Nr fertilization [2,3], resulting in the high NH₃ concentrations in the atmosphere. NH₃ increase has enhanced the acidification and eutrophication of the ecosystems on local and international scales [2,4]. Previous studies have shown that the lifetime of NH₃ is very short from hours to several days [5,6] converting to particulate matter (PM) as well as leading to dry and wet depositions. NH₃ reacts with acid-forming compounds such as sulfur

dioxide (SO₂) and nitrogen oxides (NO_x) to form particles containing ammonium sulfate ((NH₄)₂SO₄) and ammonium nitrate (NH₄NO₃) in the atmosphere [7]. These processes increase the amount of atmospheric particulate matter, particularly for particles smaller than 2.5 micrometers in diameter (PM_{2.5}), thereby reducing visibility and negatively affecting environmental and human health [8,9]. Therefore, monitoring the ground NH₃ concentrations on a regional scale is vitally important to assist in enacting effective measures to protect the eco-environments and public health, with respect to air, soil, and water quality.

Progress in the understanding of the NH₃ cycling process, flux measurements, and instrumentation have allowed advances in estimating NH₃ concentrations in the atmosphere on a local or regional scale, based on the simulation of the chemical transport models (CTM). For example, a coupled MM5-CMAQ modeling system was used for computing the ground NH₃ concentration based on the NH₃ emission developed with a spatial resolution of 27 km × 27 km in the Beijing–Tianjin–Hebei (BTH) region of China [10]. The simulation error of ground NH₃ concentration in different seasons in BTH range from −24.4% to 7.8%, indicating the ground NH₃ concentrations simulated by MM5-CMAQ are comparable with the observations; A GEOS-Chem model was used to estimate the global and seasonal NH₃ with a resolution of 2° latitude × 2.5° longitude [11], showing that the simulated ground NH₃ concentrations are biased low compared to the Tropospheric Emission Spectrometer (TES) with seasonal mean differences of −0.92 to 1.58 ppb. Similar reports on estimating ground NH₃ concentrations from CMT could also be tracked in several studies [12–14]. Although these CTMs could simulate the profiles of NH₃ concentrations in the atmosphere, the ground NH₃ concentrations over a large scale, such as on a national scale over the entire area of China, are still poorly understood due to the large pixel sizes and the relatively high uncertainties resulting from errors of the emission data and the simplification of the chemistry schemes. Fortunately, numerous studies have shown that CTMs can produce profiles for aerosol [15–18], NO₂ [19–21], NH₃ [2,22–24], and SO₂ [19,25], denoting that the vertical profiles of the NH₃ concentrations from CTM were highly beneficial in calculating the ground NH₃ concentrations.

In comparison with CTM simulations, satellite remote sensing is considered as an observational perspective and offers another way to obtain large-scale NH₃ columns with high spatial resolutions, based on advanced infrared spectroscopy (IR) sounders, such as the Infrared Atmospheric Sounding Interferometer (IASI), the Tropospheric Emission Spectrometer (TES), and the Cross-track Infrared Sounder (CrIS) [26,27]. Large-scale distributions of IASI NH₃ columns could denote the status of NH₃ levels in regions not covered by ground measurement networks, expanding insight into new NH₃ sources including industry, agriculture, and biomass burning [2,22]. However, satellite NH₃ can only provide the columns and has no information of the vertical distributions of the columns (from the ground to the top of the atmosphere), presenting a barrier in obtaining the ground NH₃ concentrations. Fortunately, as mentioned in the last paragraph, the detailed NH₃ profiles could be obtained from CTMs. Combining the advantages of CTMs (NH₃ profiles) and satellite observations (large-scale overages with high spatiotemporal resolutions), the ground NH₃ concentrations can be derived.

We aimed to generate spatiotemporal ground NH₃ concentrations with the aid of the remotely sensed NH₃ columns and vertical NH₃ profiles from a CTM. The estimated ground NH₃ concentrations were further compared with the national ground monitoring network of the Chinese Nationwide Nitrogen Deposition Monitoring Network (NNDMN). Our purpose is not to replace traditional algorithms, but to combine the advantages of satellite with high spatial and temporal resolutions, and CTMs with detailed NH₃ vertical profiles in order to obtain high spatiotemporal ground NH₃ concentrations over China, hence providing basic information for the ground status of NH₃ concentrations and guiding the monitoring plans in the future over China.

2. Materials and Methods

2.1. Ground NH_3 Concentrations in the Atmosphere

Monitoring ground-based NH_3 concentrations on a regional scale is not straightforward due to the technical limitations and great variability of the concentrations in time and space [28]. While the availability of NH_3 concentration data and the flux measurements on local scales is increasing, the measurements on a regional scale are sparser [1].

We used the monthly ground NH_3 concentrations from the Chinese Nationwide Nitrogen Deposition Monitoring Network (NNDMN, made available on request by Prof. X.J. Liu, China Agricultural University) to evaluate the accuracy of the satellite-derived ground NH_3 concentrations. Monthly NH_3 concentrations (in units of $\mu\text{g N m}^{-3}$) were measured at 44 sites from 2010 to 2013 (Figure 1). The network mainly covered farmland sites but also included some grassland (two) and forest (four) sites across China [29,30]. The ground NH_3 concentrations in NNDMN were monitored using both DENuder for Long-Term Atmospheric (DELTA) systems as well as Adapted Low-cost, Passive High Absorption (ALPHA) samplers [30,31]. ALPHA is a passive sampling system, while DELTA is an active sampling system. Monthly ground NH_3 concentrations were mostly monitored by DELTA, and few monitoring sites were measured by ALPHA. Xu et al. [30] showed that these two methods on measuring ground NH_3 concentrations were not significantly different and can be considered consistent.

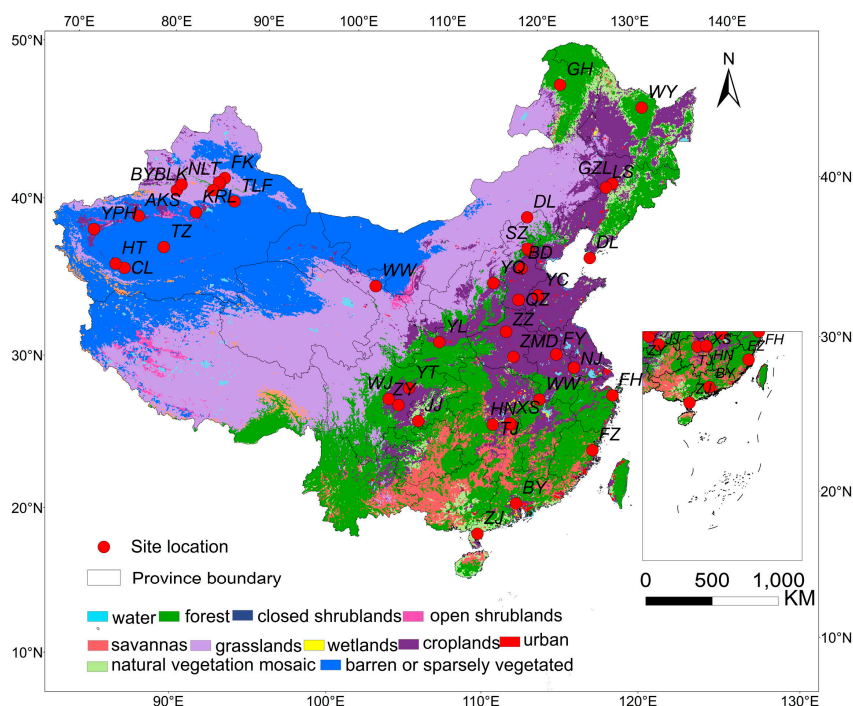


Figure 1. Spatial distribution of ground monitoring NH_3 sites in the Chinese Nationwide Nitrogen Deposition Monitoring Network (NNDMN).

2.2. IASI NH_3 Columns

The IASI instrument is on board the polar sun-synchronous MetOp platform, which crosses the equator at a mean local solar time of 9.30 a.m. and p.m. [32]. In this study, we used the measurements from the morning overpass as they are generally more sensitive to NH_3 because of higher thermal contrast at this time of day [1]. IASI has an elliptical footprint of 12 km by 12 km (at nadir) and up to 20 km by 39 km (off nadir), depending on the satellite viewing angle. The availability of measurements is mainly dependent on the cloud coverage.

The current method is based on the calculation of a spectral hyperspectral range index and subsequent conversion to a NH_3 total column using a neural network. Details on the retrieval algorithms can be found in Whitburn et al. [32]. We requested the IASI NH_3 data from Université Libre De Bruxelles, and processed the daily observation data to monthly average data for deriving the ground NH_3 . In the present work, the observations with a cloud coverage lower than 25%, and relative error lower than 100% or absolute error less than $5 \times 15 \text{ molec. cm}^{-2}$ were processed [27].

2.3. NH_3 Profiles from MOZART-4

MOZART-4 (Model for Ozone and Related chemical Tracers, version 4) is a three-dimensional (3-D) global chemical transport model simulating the chemical and transport processes, which can be driven by essentially any meteorological dataset and with any emissions inventory [24,33]. The MOZART-4 used in this study includes detailed chemistry, an improved scheme for the determination of albedo, aerosols, online calculations of photolysis rates, dry deposition, H_2O concentration, and biogenic emissions. A comprehensive tropospheric chemistry with 85 gas-phase species, 12 bulk aerosol species, 39 photolyses, and 157 gas-phase reactions has been included in MOZART-4 [24]. The chemical initial and boundary conditions, spatially and temporally varying (6 h), are constrained by global chemical transport simulations from MOZART-4/GEOS-5 (Goddard Earth Observing System-5) with 1.9° latitude \times 2.5° longitude horizontal resolution and 56 vertical levels from the surface. Details on the meteorological data and emission inventory used for driving MOZART-4 as well as related configurations can be tracked in Emmons et al. [24]. We requested the MOZART output data from NCAR (National Center for Atmospheric Research, Boulder, CO, USA). The output data are varying 6 h (daily). We calculated the monthly data by averaging the daily data, and then used the monthly data for analysis.

2.4. Satellite Derived Ground NH_3 Measurements

The fundamental thoughts of the methodology in this work were demonstrated in previous studies for aerosol [15–17], NO_2 [19–21] and SO_2 [19,25]. The recent progress in satellite NH_3 measurements also made this methodology applicable in estimating the ground NH_3 concentrations by combining the NH_3 profiles from CTM and NH_3 columns.

We had three major steps to estimate the satellite-derived ground NH_3 concentrations (Figure 2). First, we produced continuous monthly IASI NH_3 columns according to the method in previous studies [27,32]. Second, we simulated the vertical profiles from MOZART-4, and calculated the ratio of ground NH_3 to NH_3 columns. Third, we derived the satellite-derived ground NH_3 concentrations combining the IASI NH_3 columns and the ratio in the second step. Of these three steps, the second step of simulating the vertical profiles was the most important and complex one. We demonstrate here the key algorithms to simulate the vertical profiles from MOZART.

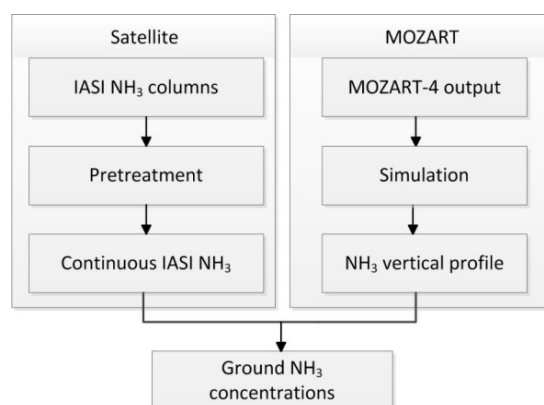


Figure 2. Schematic of the method to estimate the satellite-derived ground NH_3 concentrations.

We retrieved the NH₃ profiles from MOZART to convert the IASI NH₃ columns to ground NH₃ concentrations. The NH₃ vertical profile function was simulated by the following equation in the grid cell using the output data from MOZART-4:

$$f(h) = \sum_{i=1}^n a_i e^{-\frac{(h-b_i)^2}{c_i^2}} \quad (1)$$

where n ranges from 2 to 6, representing the number of Gaussian items; a_i , b_i , and c_i indicate the constants for each Gaussian item; h indicates the vertical height from the ground and $f(h)$ is the NH₃ concentration at height h . Theoretically, we can use n larger than 6 (with more Gaussian items). However, it is highly dependent on the computational time cost and computer memory limitations.

We simulated the NH₃ vertical profile using Equation (1) by each grid cell, based on the 56 vertical layers of NH₃ concentrations from MOZART. For each grid cell, we had five models ($n = 2, 3, 4, 5, 6$) and used R^2 and root-mean-square error (RMSE) to assess each model performance. We selected the best one with highest R^2 and lowest RMSE (i.e., determined the value of n).

The MOZART NH₃ columns can be gained by integration based on the simulated profile function:

$$F(h_{trop}) = \int_0^{h_{trop}} f(h) dh \quad (2)$$

where $F(h_{trop})$ denotes NH₃ columns and h_{trop} indicates the tropospheric height.

The satellite-derived ground NH₃ concentration is calculated as:

$$[{}_S\text{NH}_3]_G = [{}_S\text{NH}_3]_{Trop} \times \frac{f(h_G)}{F(h_{trop})} \quad (3)$$

where $[{}_S\text{NH}_3]_{Trop}$ indicates the IASI NH₃ columns, $f(h_G)$ denotes the ground NH₃ concentration from MOZART, and $F(h_{trop})$ represents the MOZART NH₃ columns.

We used the national ground-based NH₃ concentrations in NNDMN between 2010–2013 to validate the satellite-derived ground NH₃ concentrations. We applied the correlation coefficient (r) and relative error ((observation-estimation)/observation) at each monitoring site to assess the accuracy of the satellite-derived ground NH₃ concentrations.

3. Results and Discussion

3.1. Accuracy Assessment of the Estimated Ground NH₃ Concentrations

To convert the IASI NH₃ columns to ground NH₃ concentrations, it is essential to obtain the vertical NH₃ profiles. We retrieved the vertical NH₃ profiles from MOZART in this study (as an example, the vertical NH₃ concentrations at five locations in January 2013 from MOZART are shown in Figure A1). The NH₃ profiles were simulated by each grid cell in China (Figure A9) with determination of coefficients (R^2) larger than 0.95 accounting for 99.81% of all grid cells (Table A1 and Figure A9). Then, we estimated the ground NH₃ concentrations based on IASI NH₃ columns and the modeling MOZART NH₃ profiles.

We used 44 ground-based sites from NNDMN between 2010–2013 to assess the performance of the estimated monthly ground NH₃ concentrations. The correlation between the estimated and measured at each site is given in Table A2 in Appendix A, and the relative bias of each site as well as the yearly comparisons between the estimated and measured ground NH₃ concentration are given in Figures 3 and 4. We found 90.91% of monitoring sites has a relative error within -30% – 50% , showing an agreement between the estimated and measured. The seasonal absolute error by inverse-distance-weighted (IDW) interpolation is also shown in Figure A2. We found the absolute error in winter (December, January, and February) was higher than in other seasons, which can be explained

by the highest relative error in IASI NH_3 columns in the winter season (Figure A3). In addition, Figure 4 demonstrates a comparison between the estimated and measured ground NH_3 concentrations before and after applying the IASI NH_3 data. We found a relatively higher correlation (R , 0.81 vs. 0.57) and a better consistency (slope, 0.96 vs. 0.50) between the satellite-derived ground NH_3 concentrations and the measured ground NH_3 concentrations than those from MOZART not applying the IASI NH_3 data.

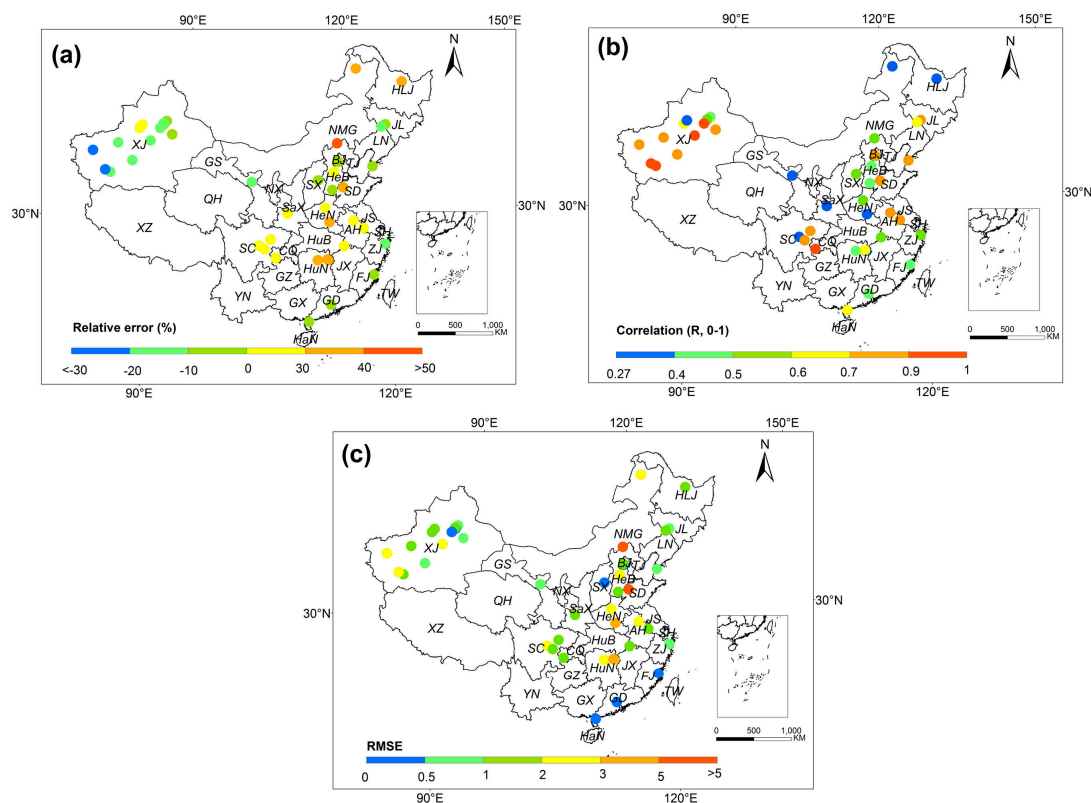


Figure 3. Spatial distribution of the relative error (a), correlation (b) and root-mean-square error (RMSE) (c) of the estimated ground NH_3 concentration ($\mu\text{g N m}^{-3}$) at 44 NNDMN sites.

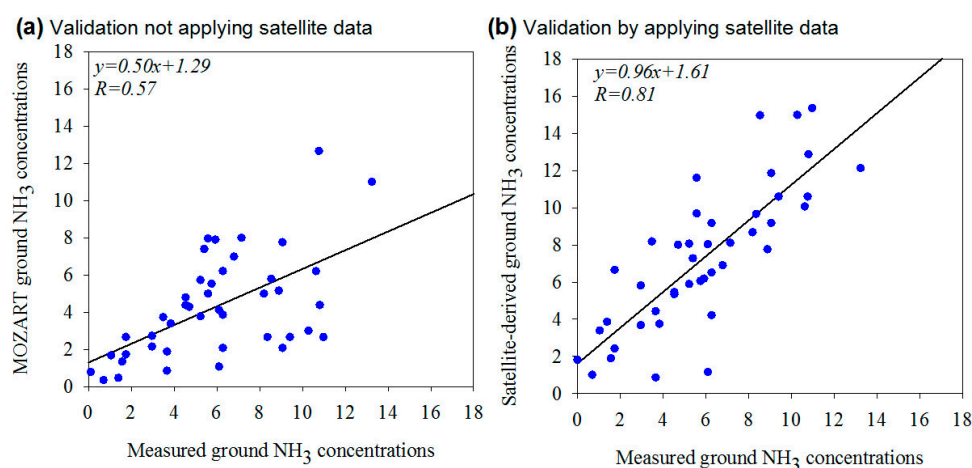


Figure 4. Yearly comparisons between the estimated and measured ground NH_3 concentration ($\mu\text{g N m}^{-3}$). (a) indicates the comparison between the measured ground NH_3 concentrations and the estimated ground NH_3 concentrations from MOZART at the lowest layer before applying the satellite data, while (b) represents the comparison between the measured and estimated ground NH_3 concentrations by applying the satellite data using the methods in Section 2.4.

3.2. Spatial Pattern of the Ground NH_3 Concentrations

Spatial distribution of ground NH_3 concentrations in 2012 over China is shown in Figure 5a. High ground NH_3 concentrations greater than $10 \mu\text{g N m}^{-3}$ were concentrated in North China and South China including Beijing–Tianjin–Hebei (BTH), Shandong, Henan, Hubei, Anhui, Sichuan and Jiangsu provinces, forming the major regions of intensive agriculture over China. Low ground NH_3 concentrations are predominantly located in TP (Tibetan Plateau), where both the synthetic fertilizers and livestock waste were the least among 32 provinces [34,35]. The spatial ground NH_3 concentrations revealed considerable spatial heterogeneity across China and were in agreement with the percent farmland area (Figure 5a,b), reflecting its unique agricultural structure and farming practice.

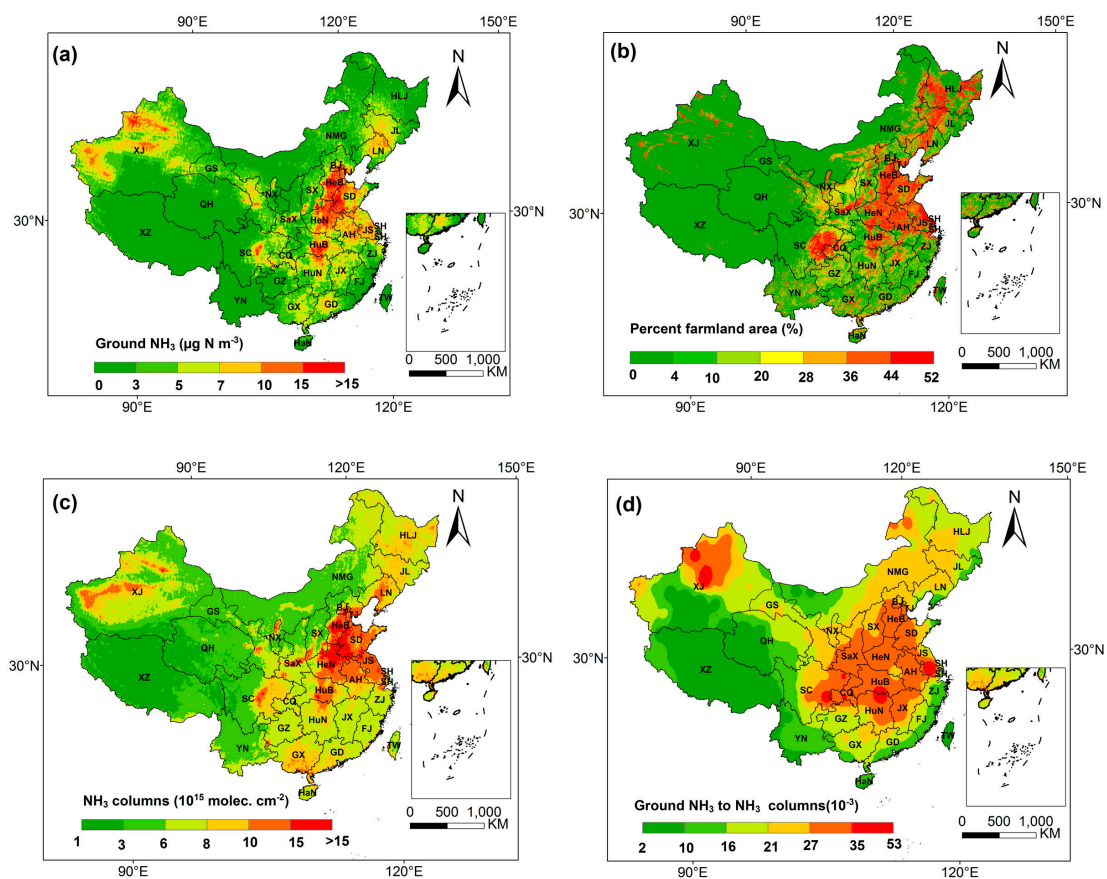


Figure 5. Spatial distribution of the ground NH_3 concentration ($\mu\text{g N m}^{-3}$). (a) represents the yearly estimated ground NH_3 concentrations; (b) denotes the percent farmland area; (c) denotes the Infrared Atmospheric Sounding Interferometer (IASI) NH_3 columns and (d) indicates the ratio of ground NH_3 concentration to NH_3 columns from MOZART.

High ground NH_3 concentrations were also observed in some areas in Xinjiang province (Figure 5a), where our estimation were about -30% to -10% underestimation compared with measurements in NNDMN (Figure 3). Moreover, relatively high NH_3 columns could be observed by satellite IASI instrument (Figure 5c). Synthetic N fertilizers and livestock waste both dominated the spatial distribution of the total emissions [34,35], hence determining the spatial patterns of the ground NH_3 concentrations. Previous studies reported that the NH_3 emissions from livestock exceeded those from the farmland in China, and NH_3 emissions from livestock accounted for about 54% of the total NH_3 emissions over China [35]. The contribution of livestock to the total NH_3 emissions in Xinjiang (where sheep are widely raised) accounted for higher than 60% [10,35]. Thus, due to the combining influence of both synthetic N fertilizers and livestock waste, the spatial distributions of ground NH_3

concentrations and percent farmland differed, especially in regions where the livestock dominated the NH_3 emissions. In addition, most of the ground NH_3 emissions were more concentrated on the ground and relatively hard to transport vertically compared with other regions in China, which can be clearly seen by the ratio of ground NH_3 concentrations to NH_3 columns from MOZART (Figure 5d).

3.3. Seasonal Variations of the Ground NH_3 Concentrations in China

To demonstrate the seasonal variations of the ground NH_3 concentrations in China, we calculated the monthly average values throughout China (Figure 6a). We found the maximum ground NH_3 concentrations over China occurred in summer (June, July, and August), followed by spring (March, April, and May), autumn (September, October, and November) and winter (December, January, and February) seasons. It is interesting that the seasonal ground NH_3 concentrations were in agreement with the seasonal patterns of NH_3 emissions in China conducted by Kang et al. [36], Huang et al. [35], and Xu et al. [37] (Figure 6b–d), indicating that the NH_3 emissions are the key factor influencing seasonal pattern of the ground NH_3 concentrations. The maximum NH_3 emissions in summer is reasonable due to more than 40% of the fertilization and more than 25% of livestock emissions occurring in summer [36,37]. In addition, high temperature in summer in China may also accelerate the NH_3 volatilization ($\text{NH}_4^+ \rightarrow \text{NH}_3 + \text{H}^+$) from fertilizer, animal waste, city garbage or vehicles [6,38–40], and hence cause high ground NH_3 concentrations. In contrast, in winter, temperature frequently below freezing leads to reduced NH_3 volatilization and lower NH_3 concentrations than in other seasons.

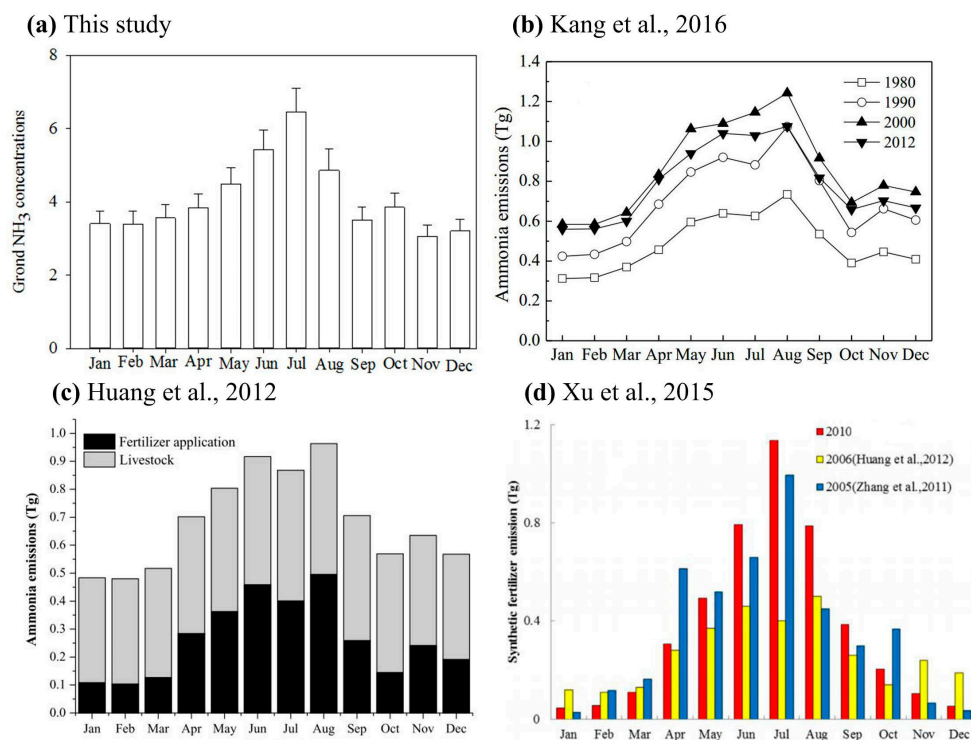


Figure 6. Seasonal patterns of ground NH_3 concentrations in China. (a) indicates the monthly variations of ground NH_3 concentrations ($\mu\text{g N m}^{-3}$) in China; (b) represents the monthly variations of the total NH_3 emissions (Tg, 10^{12} g) in China conducted by Kang et al. [36]; (c) shows the the monthly variations of the sum of fertilizer and livestock NH_3 emissions (Tg) in China conducted by Huang et al. [35] and (d) denotes the monthly variations of the fertilizer NH_3 emissions (Tg) in China conducted by Xu et al. [37].

To more accurately quantify the effects of meteorological parameters on the seasonal trends of the ground NH_3 concentrations, we selected the five best-simulated ground sites with $n > 30$

(Table A2) for demonstrating meteorological parameters, such as temperature, wind speed, humidity, and precipitation on the seasonal variations of the ground NH_3 concentrations (Figures 7 and A4–A8). The monthly wind speed, temperature, relative humidity, and precipitation for each site were taken from the China Meteorological Administration. A positive correlation ($R = 0.6$, $p = 0.00$) was found between the ground NH_3 concentrations and temperature. An inverse relationship between the ground NH_3 concentrations and humidity (Figure 7), indicated that higher relative humidity may contribute to more NH_3 loss rates ($\text{NH}_3 \rightarrow \text{NH}_4^+$). In addition, we also conducted a partial correlation analysis [41] regarding ground NH_3 concentrations, temperature, and humidity by considering their interactions using the function “partialcorr” in Matlab. We found the partial correlation between ground NH_3 concentrations and humidity was -0.10 ($p = 0.03$), showing a significant inverse relationship between the ground NH_3 concentrations and humidity. Significant effects of air humidity on NH_3 loss were also demonstrated previously [42,43]. However, precipitation and wind speed were not significantly correlated with ground NH_3 concentrations ($p = 0.632$, precipitation vs. NH_3 ; $p = 0.156$, wind speed vs. NH_3) as shown in Figures A4–A8.

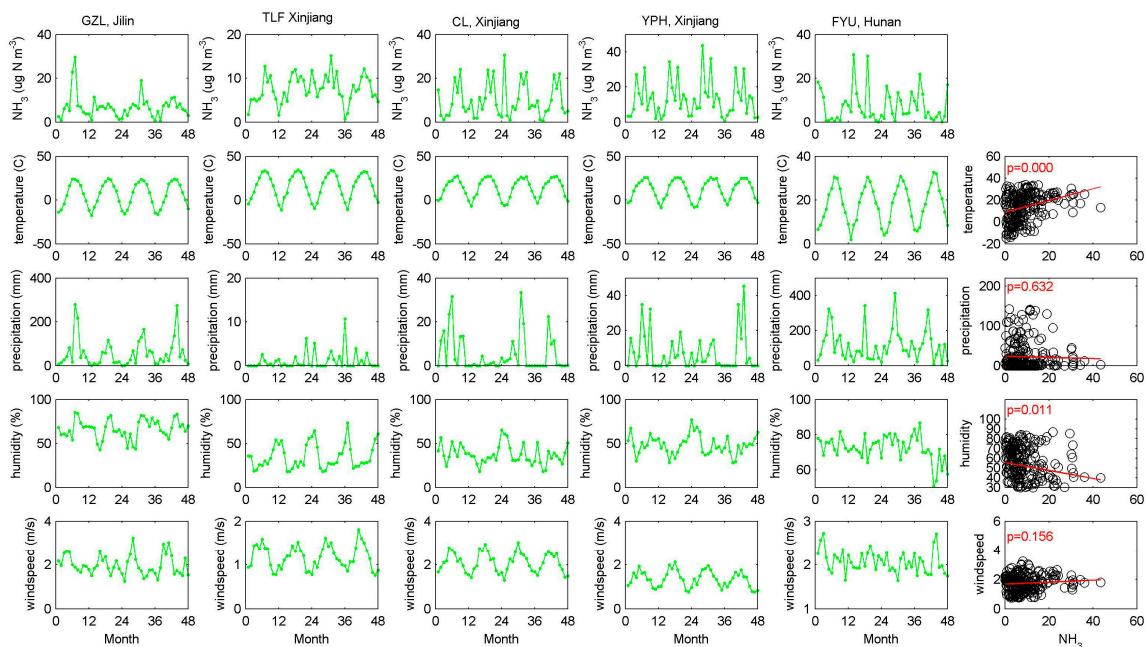


Figure 7. The seasonal variations of ground NH_3 concentrations ($\mu\text{g N m}^{-3}$), temperature ($^{\circ}\text{C}$), precipitation (mm), humidity (%), and wind speed (m/s) at five sites with best-simulated ground NH_3 concentrations from January 2010 to December 2013 (0–12, 2010; 13–24, 2011; 25–36, 2012; 37–48, 2013). The relationship between the ground NH_3 concentrations and precipitation (mm), humidity (%), and wind speed (m/s) at each site is provided in Figures A4–A8.

3.4. Comparison with Previous Studies

The first relatively complete work on the national ground measurements of NH_3 concentrations in China is NNDMN, and the results of ground measurements were published by Xu et al. [30], which we considered as a truly comprehensive and valuable work on the national status of the ground NH_3 concentrations, and which shed some light on the actual status of ground NH_3 concentrations. The national measurements in NNDMN provide the best accurate datasets for validating the modeling ground NH_3 concentrations. In the previous studies, due to very limited ground measurements (not to mention the national monitoring measurements), it was difficult to validate the accuracy of the modeling ground NH_3 concentrations in China. The lack of measurements makes it necessary to assess the modeling ground NH_3 concentrations in China [44]. Recently, Zhao et al. [45] presented

a comprehensive work on the national-scale model validation of ground NH_3 concentrations with $1/2^\circ$ longitude by $1/3^\circ$ latitude horizontal resolution using the GEOS-Chem model, showing the correlation coefficient with NNDMN between 2011–2012 which was about 0.65 on the annual scale [45]. Compared with Zhao et al. [45], we used the same datasets from NNDMN while having a longer time period (2010–2013) to validate our estimated ground NH_3 concentrations, and found the correlation coefficient was about 0.81 (slope = 0.96 and intercept = 1.31) on the annual scale as shown in Figure 4, demonstrating better agreement with the ground measurements. The relatively higher accuracy in estimating ground NH_3 concentrations may result from different datasets used for estimation, where we used the satellite observation and Zhao et al. [45] used the NH_3 emission data used for modeling. Uncertainties existed in the estimation of NH_3 emission resulting from the methodology of calculation, which simplified the complexity of the real status of emission process [36]. For example, *N*-fertilizer NH_3 emission in BTH between different studies varied greatly as 256.5 Gg [35], 502.5 Gg [46], 432.7 Gg [10]; livestock NH_3 emission in BTH between different studies varied as 556.6 Gg [35], 675.2 Gg [46], and 891.6 Gg [10]. The estimation of NH_3 emissions by Zhou et al. [10] even nearly doubled that by Huang et al. [35] and Dong et al. [46]. The actual local emission factors in different regions differed from each other greatly, due to the difference of the local meteorological conditions, fertilizing time, and fertilizer kinds [37]. The NH_3 emissions are mainly based on statistical NH_3 emissions at a city or county level, and the accuracy is strongly dependent on both the limited spatial and temporal resolutions of the coarse statistical data [35–37,44,47].

The present study derived ground NH_3 concentrations from IASI NH_3 columns and the profiles from MOZART-4, implying that a combination of CTM modeling and satellite monitoring obtained a reliable ground NH_3 estimation over China. More generally, this attempt to generate the ground NH_3 measurements with a relative high resolution from IASI and MOZART has highlighted known limitations in the ground NH_3 monitoring measurements, which may in some cases not be representative of the estimated NH_3 concentrations horizontally and vertically. Here we highlight the need to acquire more comprehensive datasets of ground NH_3 concentrations, and dedicated measurement campaigns focusing on the ground NH_3 measurement will no doubt allow improvements in the validation of estimated NH_3 in the future. In addition, we focused on the spatial pattern of ground NH_3 concentrations derived from satellite and a CTM, which is based on the monthly average and may be limited for the specific analysis such as secondary aerosol formation, photochemistry, and consideration of regulation. It is also beneficial and even essential to gain higher temporal resolution of ground NH_3 concentrations in the future.

4. Conclusions

We critically estimated the ground NH_3 concentrations over China, combining IASI NH_3 columns and NH_3 profiles from MOZART. We aimed to generate ground NH_3 concentrations over China, and hence provide potential to understand both the spatial and temporal variations of ground NH_3 concentrations in order to guide future ground NH_3 monitoring plans. The intention was not to replace traditional algorithms but to provide new insight on the current status of ground NH_3 over China, and to generate more reliable ground NH_3 concentrations. The IASI NH_3 columns and NH_3 profiles from the atmospheric chemistry transport model are encouraged to be combined to generate ground NH_3 concentrations at local or regional scales, and the estimated results should be further improved.

This study introduced methods to estimate ground NH_3 concentrations over China using IASI NH_3 columns and NH_3 profiles. The estimated ground NH_3 concentrations were validated by 44 sites from NNDMN, showing promising results between the estimated and measured, and then the spatial and temporal variations of ground NH_3 concentrations were demonstrated. High ground NH_3 concentrations greater than $10 \mu\text{g N m}^{-3}$ were mainly located in Beijing, Hebei, Shandong, Henan, Jiangsu, eastern Sichuan, and some regions in Xinjiang provinces, while low ground NH_3 concentrations were concentrated in the Tibet-Plateau area. The maximum ground NH_3 concentrations

over China occurred in summer, followed by spring, autumn, and winter seasons, which are in agreement with the seasonal patterns of NH_3 emissions in China.

Acknowledgments: This study was supported by the National Natural Science Foundation of China (No. 41471343, 40425007 and 41101315) and Doctoral Research Innovation Fund (2016CL07). We also much appreciate the free use of the IASI NH_3 data provided by Université Libre de Bruxelles (ULB) (<http://www.ulb.ac.be/cpm/atmosphere.html>).

Author Contributions: L.L. and X.Z. conceived the idea; L.L. and S.W. conducted the analyses; L.L. and S.W. processed the data; X.L. and W.X. provided the observation data for validation; X.Z., X.L., L.Z., and W.Z. contributed to the writing and revisions.

Conflicts of Interest: The authors declare no competing financial interest.

Appendix A

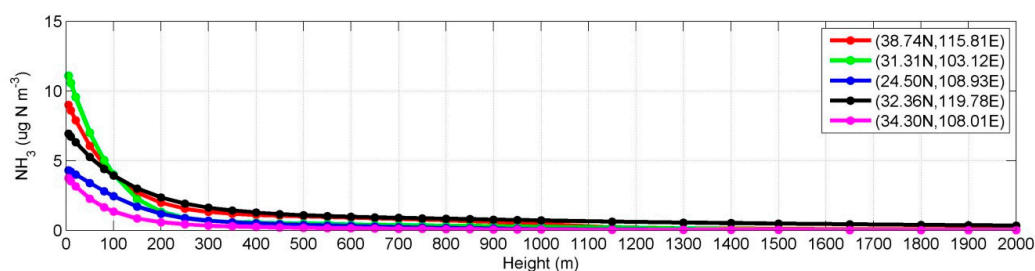


Figure A1. Vertical NH_3 concentrations ($\mu\text{g N m}^{-3}$) simulated by Mozart at five locations in January 2013.

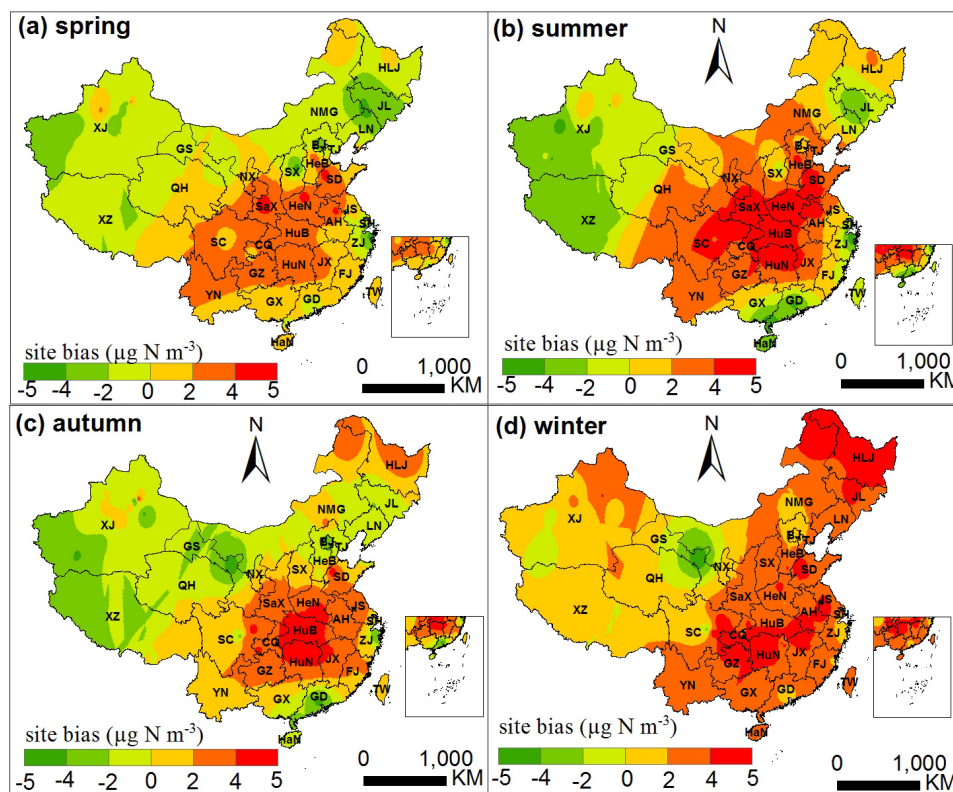


Figure A2. A quick illustration of the site bias of ground NH_3 concentrations across China by interpolating the residuals between the measured and estimated using the inverse-distance-weighted (IDW) interpolation. The figures were generated using ArcGIS 12.0 software (<https://www.arcgis.com/>).

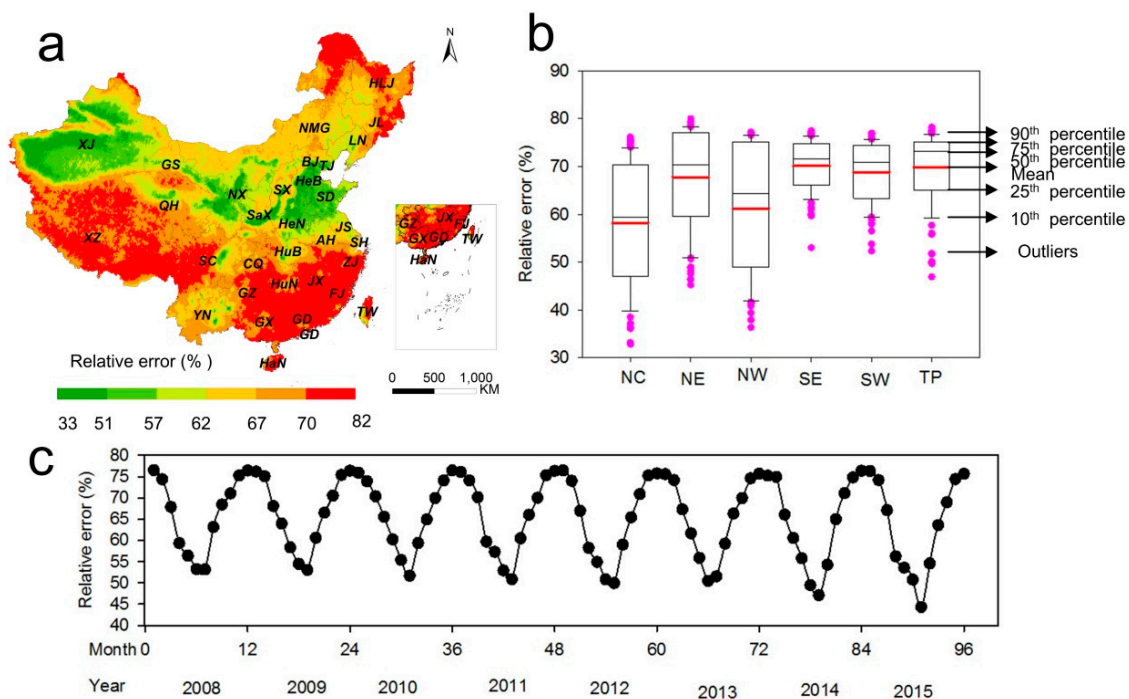


Figure A3. Relative error (%) of IASI NH₃ columns. (a) indicates the annual IASI NH₃ error (with a cloud coverage lower than 25%) averaged from 2008 to 2015; (b) indicates the averaged monthly relative error from 2008 to 2015 in different regions (every dot indicates the relative error at a month in a region); (c) indicates the temporal variations of relative error over China at a monthly scale.

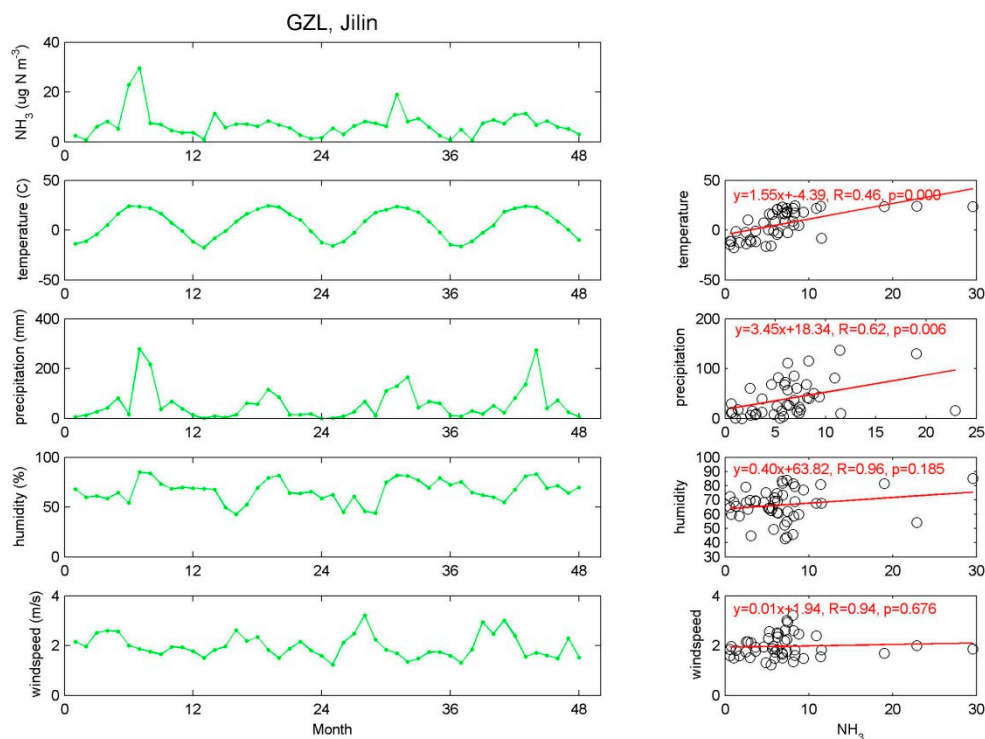


Figure A4. The seasonal variations of ground NH₃ concentrations ($\mu\text{g N m}^{-3}$), temperature (°C), precipitation (mm), humidity (%), and wind speed (m/s) at GZL from January 2010 to December 2013 (0–12, 2010; 13–24, 2011; 25–36, 2012; 37–48, 2013).

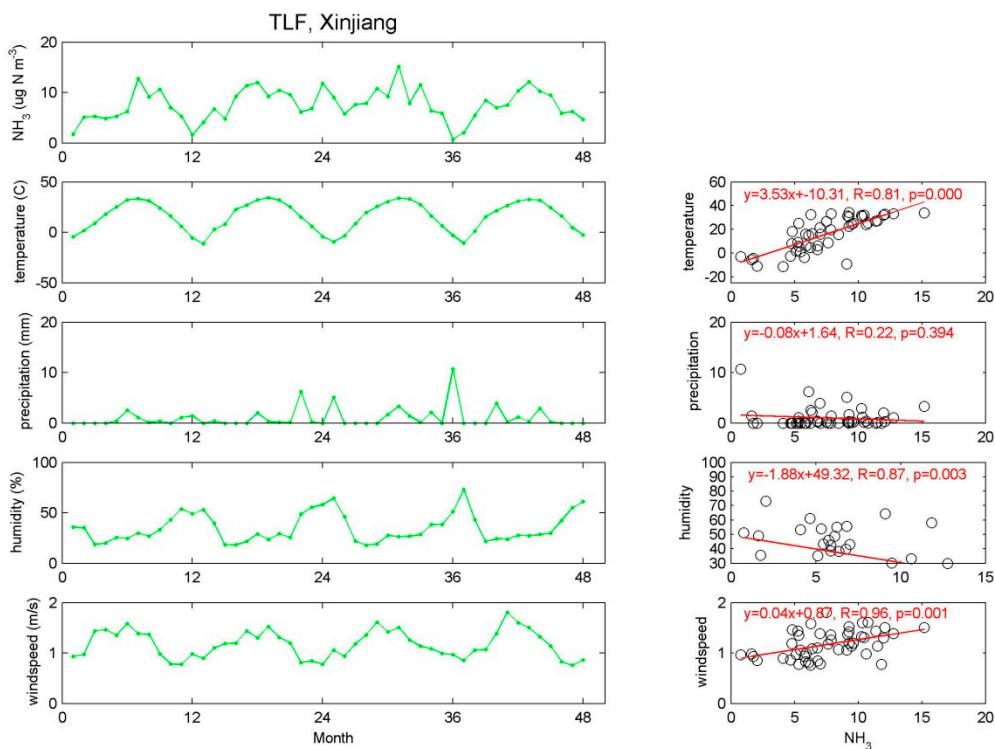


Figure A5. The seasonal variations of ground NH_3 concentrations ($\mu\text{g N m}^{-3}$), temperature ($^{\circ}\text{C}$), precipitation (mm), humidity (%), and wind speed (m/s) at TLF from January 2010 to December 2013 (0–12, 2010; 13–24, 2011; 25–36, 2012; 37–48, 2013).

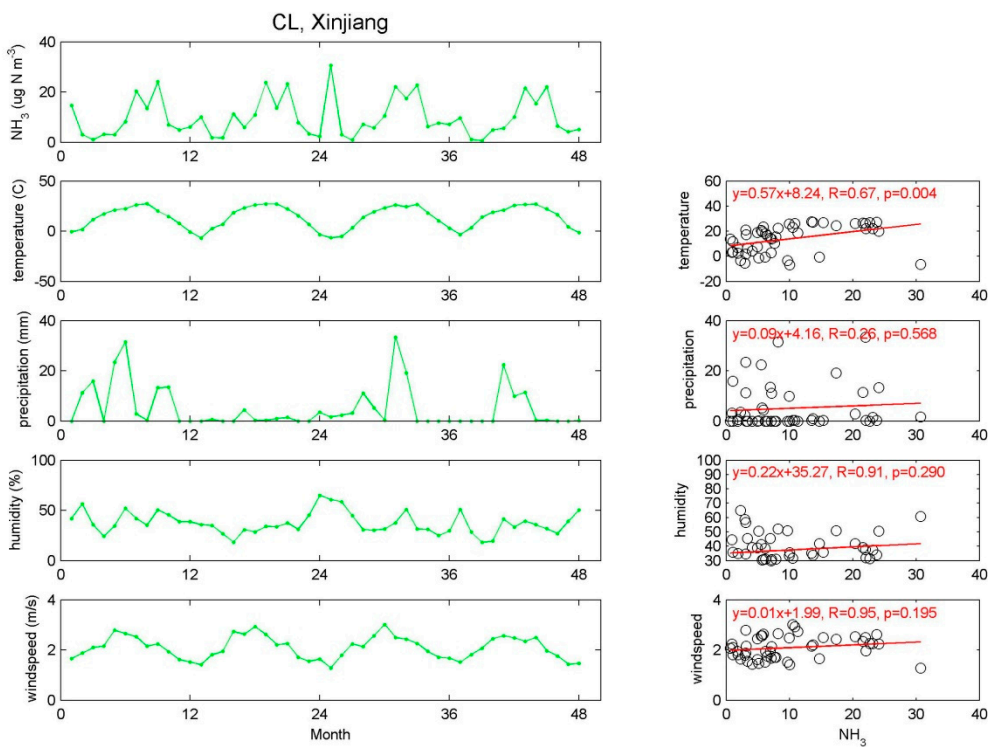


Figure A6. The seasonal variations of ground NH_3 concentrations ($\mu\text{g N m}^{-3}$), temperature ($^{\circ}\text{C}$), precipitation (mm), humidity (%), and wind speed (m/s) at CL from January 2010 to December 2013 (0–12, 2010; 13–24, 2011; 25–36, 2012; 37–48, 2013).

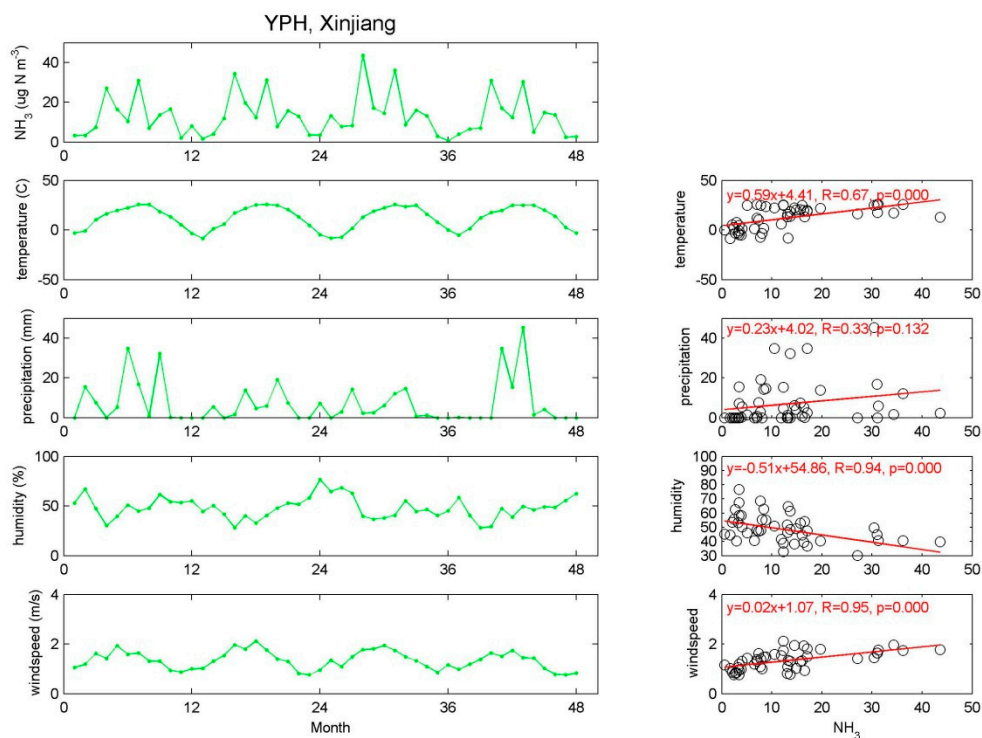


Figure A7. The seasonal variations of ground NH_3 concentrations ($\mu\text{g N m}^{-3}$), temperature ($^{\circ}\text{C}$), precipitation (mm), humidity (%), and wind speed (m/s) at YPH from January 2010 to December 2013 (0–12, 2010; 13–24, 2011; 25–36, 2012; 37–48, 2013).

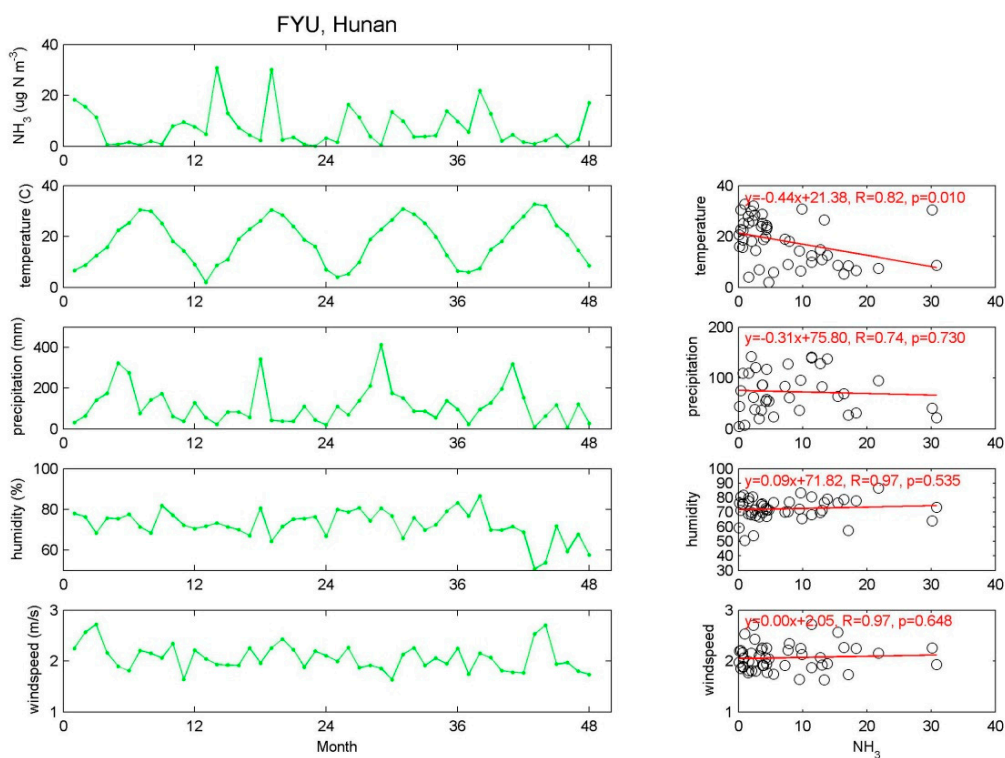


Figure A8. The seasonal variations of ground NH_3 concentrations ($\mu\text{g N m}^{-3}$), temperature ($^{\circ}\text{C}$), precipitation (mm), humidity (%), and wind speed (m/s) at FYU from January 2010 to December 2013 (0–12, 2010; 13–24, 2011; 25–36, 2012; 37–48, 2013).

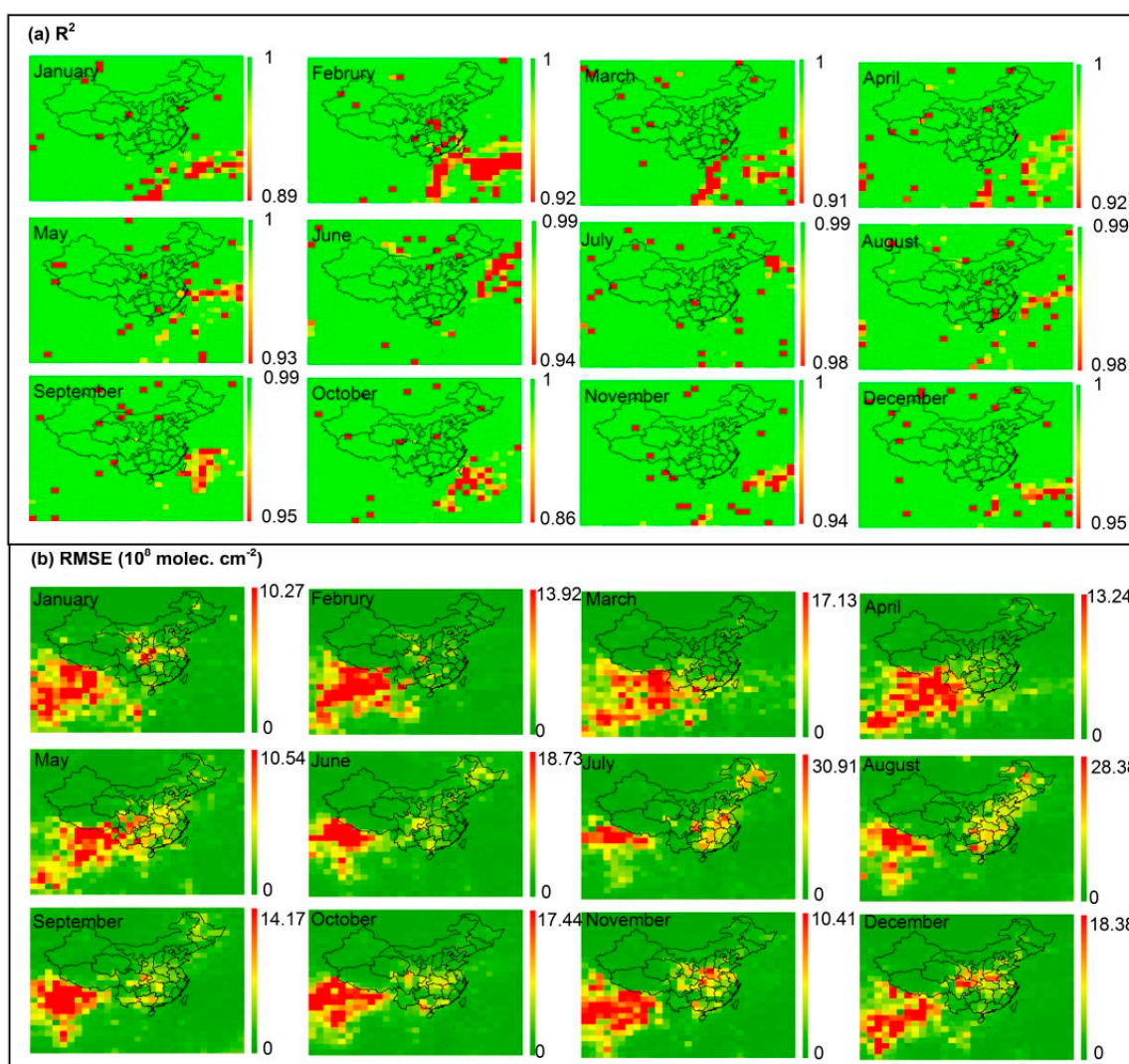


Figure A9. (a,b) R^2 and RMSE (molec./cm^2) for the Gaussian simulation of the NH_3 profiles ($68\sim 142^\circ\text{E}$, $5\sim 55^\circ\text{N}$) in 2013.

Table A1. Descriptive statistics for results of Gaussian simulation.

Season (%)	$N = 2$	$N = 3$	$N = 4$	$N = 5$	$N = 6$	$R^2 > 0.95$	$R^2 > 0.99$
Spring	0.70	12.02	33.33	34.61	19.31	99.86	96.94
Summer	0.79	10.47	28.24	37.09	23.38	99.86	97.52
Autumn	0.48	7.60	24.58	37.93	29.39	99.86	98.89
Winter	0.92	10.25	31.03	35.80	21.97	99.64	96.46
All	0.72	10.09	29.29	36.36	23.51	99.81	97.45

Note: Spring includes March, April, and May; Summer includes June, July, and August; Autumn includes September, October, and November; Winter includes December, January, and February. N indicates the numbers of the Gaussian items. For details, please refer to the methods part.

Table A2. Comparison between monthly IASI satellite-derived ground NH₃ concentrations and the NNDMN monitoring sites from 2010 to 2013.

Site	Landuse	Long (°E)	Lat (°N)	n	R (±std)
					This Study
BYBLK	Alpine grassland	83.71	42.88	22	0.68 (0.05)
FK	Desert-oasis ecotone	87.93	44.29	32	0.49 (0.04)
TLF	Desert in an oasis	89.19	42.85	28	0.84 (0.07)
SDS	Urban	87.56	43.85	38	0.69 (0.06)
TFS	Suburban	87.47	43.94	35	0.56 (0.05)
CL	Desert-oasis ecotone	80.73	37.02	12	0.94 (0.08)
TZ	Desert	83.66	38.97	12	0.89 (0.07)
YPH	Farmland	77.27	39	12	0.83 (0.05)
HT	Farmland	79.89	37.15	5	0.99 (0.08)
AKS	Farmland	80.83	40.62	17	0.72 (0.06)
KRL	Farmland	85.86	41.68	6	0.94 (0.08)
NLT	Forest	84.03	43.31	4	0.33 (0.03)
NSXC	Forest	87.04	43.35	7	0.98 (0.09)
CAU	Urban	116.28	40.02	45	0.57 (0.05)
ZZ	Urban	113.63	34.75	44	0.55 (0.04)
SZ	Farmland	116.2	40.11	45	0.86 (0.07)
BD	Farmland	115.48	38.85	12	0.44 (0.04)
QZ	Farmland	114.94	36.78	45	0.50 (0.04)
YQ	Farmland	112.89	38.05	45	0.57 (0.05)
ZMD	Farmland	114.05	33.02	45	0.27 (0.02)
YL	Farmland	108.01	34.31	45	0.27 (0.02)
YC	Farmland	116.63	36.94	35	0.77 (0.06)
GZL	Farmland	124.83	43.53	42	0.82 (0.06)
LS	Farmland	124.17	43.36	42	0.62 (0.05)
DL	Coastal	121.58	38.92	40	0.73 (0.05)
WY	Forest	129.25	48.11	12	0.31 (0.02)
GH	Forest	121.52	50.78	12	0.38 (0.03)
WW	Farmland	102.6	38.07	39	0.32 (0.02)
DL	Grassland	116.49	42.2	6	0.52 (0.04)
WX	Farmland	115.79	30.01	29	0.56 (0.05)
BY	Farmland	113.27	23.16	44	0.47 (0.04)
TJ	Farmland	111.97	28.61	39	0.42 (0.03)
FYU	Farmland	113.34	28.56	40	0.76 (0.06)
HN	Farmland	113.41	28.52	40	0.36 (0.03)
NJ	Farmland	118.85	31.84	18	0.82 (0.06)
FY	Farmland	117.56	32.88	11	0.79 (0.06)
ZJ	Coastal	110.33	21.26	41	0.63 (0.05)
FZ	Coastal	119.36	26.17	45	0.49 (0.03)
FH	Coastal	121.53	29.61	41	0.57 (0.04)
XS	Forest	113.31	28.61	40	0.67 (0.06)
WJ	Farmland	103.84	30.55	39	0.28 (0.02)
ZY	Farmland	104.63	30.13	42	0.74 (0.06)
YT	Farmland	105.47	31.28	30	0.78 (0.06)
JJ	Farmland	106.18	29.06	12	0.94 (0.08)

References

1. Van Damme, M.; Clarisse, L.; Dammers, E.; Liu, X.; Nowak, J.; Clerbaux, C.; Flechard, C.; Galy-Lacaux, C.; Xu, W.; Neuman, J.; et al. Towards validation of ammonia (NH₃) measurements from the IASI satellite. *Atmos. Meas. Tech.* **2014**, *7*, 12125–12172. [[CrossRef](#)]
2. Warner, J.; Wei, Z.; Strow, L.; Dickerson, R.; Nowak, J. The global tropospheric ammonia distribution as seen in the 13 year AIRS measurement record. *Atmos. Chem. Phys. Discuss.* **2015**, *15*, 35823–35856. [[CrossRef](#)]

3. Van Damme, M.; Wichink Kruit, R.; Schaap, M.; Clarisse, L.; Clerbaux, C.; Coheur, P.F.; Dammers, E.; Dolman, A.; Erismann, J. Evaluating 4 years of atmospheric ammonia (NH₃) over Europe using IASI satellite observations and LOTOS-EUROS model results. *J. Geophys. Res. Atmos.* **2014**, *119*, 9549–9566. [[CrossRef](#)]
4. Paulot, F.; Jacob, D.J.; Pinder, R.; Bash, J.; Travis, K.; Henze, D. Ammonia emissions in the United States, European Union, and China derived by high-resolution inversion of ammonium wet deposition data: Interpretation with a new agricultural emissions inventory (MASAGE_NH₃). *J. Geophys. Res. Atmos.* **2014**, *119*, 4343–4364. [[CrossRef](#)]
5. Kruit, R.J.W.; Schaap, M.; Sauter, F.J.; Zanten, M.C.V. Modeling the distribution of ammonia across Europe including bi-directional surface-atmosphere exchange. *Biogeosciences* **2012**, *9*, 5261–5277. [[CrossRef](#)]
6. Sutton, M.A.; Reis, S.; Riddick, S.N.; Dragosits, U.; Nemitz, E.; Theobald, M.R.; Tang, Y.S.; Braban, C.F.; Vieno, M.; Dore, A.J.; et al. Towards a climate-dependent paradigm of ammonia emission and deposition. *Philos. Trans. R. Soc. B Biol. Sci.* **2013**, *368*. [[CrossRef](#)] [[PubMed](#)]
7. Gu, B.; Sutton, M.A.; Chang, S.X.; Ge, Y.; Chang, J. Agricultural ammonia emissions contribute to China's urban air pollution. *Front. Ecol. Environ.* **2014**, *12*, 265–266. [[CrossRef](#)]
8. Gu, B.; Ge, Y.; Ren, Y.; Xu, B.; Luo, W.; Jiang, H.; Gu, B.; Chang, J. Atmospheric reactive nitrogen in China: Sources, recent trends, and damage costs. *Environ. Sci. Technol.* **2012**, *46*, 9420–9427. [[CrossRef](#)] [[PubMed](#)]
9. Pope, C.A., III; Burnett, R.T.; Thun, M.J.; Calle, E.E.; Krewski, D.; Ito, K.; Thurston, G.D. Lung cancer, cardiopulmonary mortality, and long-term exposure to fine particulate air pollution. *JAMA* **2002**, *287*, 1132–1141. [[CrossRef](#)] [[PubMed](#)]
10. Zhou, Y.; Shuiyuan, C.; Lang, J.; Chen, D.; Zhao, B.; Liu, C.; Xu, R.; Li, T. A comprehensive ammonia emission inventory with high-resolution and its evaluation in the Beijing–Tianjin–Hebei (BTH) region, China. *Atmos. Environ.* **2015**, *106*, 305–317. [[CrossRef](#)]
11. Luo, M.; Shephard, M.W.; Cady-Pereira, K.E.; Henze, D.K.; Zhu, L.; Bash, J.O.; Pinder, R.W.; Capps, S.L.; Walker, J.T.; Jones, M.R. Satellite observations of tropospheric ammonia and carbon monoxide: Global distributions, regional correlations and comparisons to model simulations. *Atmos. Environ.* **2015**, *106*, 262–277. [[CrossRef](#)]
12. Hamaoui-Laguel, L.; Meleux, F.; Beekmann, M.; Bessagnet, B.; Générumont, S.; Cellier, P.; Létinois, L. Improving ammonia emissions in air quality modelling for France. *Atmos. Environ.* **2014**, *92*, 584–595. [[CrossRef](#)]
13. Wen, D.; Zhang, L.; Lin, J.; Vet, R.; Moran, M. An evaluation of ambient ammonia concentrations over southern Ontario simulated with different dry deposition schemes within STILT-Chem v0.8. *Geosci. Model Dev.* **2014**, *7*, 1037–1050. [[CrossRef](#)]
14. Wen, D.; Lin, J.; Zhang, L.; Vet, R.; Moran, M. Modeling atmospheric ammonia and ammonium using a stochastic Lagrangian air quality model (STILT-Chem v0.7). *Geosci. Model Dev.* **2013**, *6*, 327–344. [[CrossRef](#)]
15. Van Donkelaar, A.; Martin, R.V.; Park, R.J. Estimating ground-level PM_{2.5} using aerosol optical depth determined from satellite remote sensing. *J. Geophys. Res. Atmos.* **2006**, *111*. [[CrossRef](#)]
16. Liu, Y.; Park, R.J.; Jacob, D.J.; Li, Q.; Kilaru, V.; Sarnat, J.A. Mapping annual mean ground-level PM_{2.5} concentrations using Multiangle Imaging Spectroradiometer aerosol optical thickness over the contiguous United States. *J. Geophys. Res. Atmos.* **2004**, *109*, 1–10.
17. Van Donkelaar, A.; Martin, R.V.; Brauer, M.; Kahn, R.; Levy, R.; Verduzco, C.; Villeneuve, P.J. Global estimates of ambient fine particulate matter concentrations from satellite-based aerosol optical depth: Development and application. *Environ. Health Perspect.* **2010**, *118*, 847. [[CrossRef](#)] [[PubMed](#)]
18. Wang, J.; Xu, X.; Spurr, R.; Wang, Y.; Drury, E. Improved algorithm for MODIS satellite retrievals of aerosol optical thickness over land in dusty atmosphere: Implications for air quality monitoring in China. *Remote Sens. Environ.* **2010**, *114*, 2575–2583. [[CrossRef](#)]
19. Nowlan, C.; Martin, R.; Philip, S.; Lamsal, L.; Krotkov, N.; Marais, E.; Wang, S.; Zhang, Q. Global dry deposition of nitrogen dioxide and sulfur dioxide inferred from space-based measurements. *Glob. Biogeochem. Cycles* **2014**, *28*, 1025–1043. [[CrossRef](#)]
20. Lamsal, L.N.; Martin, R.V.; van Donkelaar, A.; Steinbacher, M.; Celarier, E.A.; Bucsela, E.; Dunlea, E.J.; Pinto, J.P. Ground-level nitrogen dioxide concentrations inferred from the satellite-borne Ozone Monitoring Instrument. *J. Geophys. Res. Atmos.* **2008**, *113*, 1–15. [[CrossRef](#)]

21. Hudman, R.C.; Jacob, D.J.; Turquety, S.; Leibensperger, E.M.; Murray, L.T.; Wu, S.; Gilliland, A.B.; Avery, M.; Bertram, T.H.; Brune, W.; et al. Surface and lightning sources of nitrogen oxides over the United States: Magnitudes, chemical evolution, and outflow. *J. Geophys. Res. Atmos.* **2007**, *112*, 1–14. [[CrossRef](#)]
22. Dammers, E.; Vigouroux, C.; Palm, M.; Mahieu, E.; Warneke, T.; Smale, D.; Langerock, B.; Franco, B.; Damme, M.V.; Schaap, M.; et al. Retrieval of ammonia from ground-based FTIR solar spectra. *Atmos. Chem. Phys.* **2015**, *15*, 12789–12803. [[CrossRef](#)]
23. Van Damme, M.; Erisman, J.W.; Clarisse, L.; Dammers, E.; Whitburn, S.; Clerbaux, C.; Dolman, A.J.; Coheur, P.F. Worldwide spatiotemporal atmospheric ammonia (NH₃) columns variability revealed by satellite. *Geophys. Res. Lett.* **2015**, *42*, 8660–8668. [[CrossRef](#)]
24. Emmons, L.; Walters, S.; Hess, P.; Lamarque, J.-F.; Pfister, G.; Fillmore, D.; Granier, C.; Guenther, A.; Kinnison, D.; Laepple, T.; et al. Description and evaluation of the Model for Ozone and Related chemical Tracers, version 4 (MOZART-4). *Geosci. Model Dev.* **2010**, *3*, 43–67. [[CrossRef](#)]
25. Lee, C.; Martin, R.V.; van Donkelaar, A.; Lee, H.; Dickerson, R.R.; Hains, J.C.; Krotkov, N.; Richter, A.; Vinnikov, K.; Schwab, J.J. SO₂ emissions and lifetimes: Estimates from inverse modeling using in situ and global, space-based (SCIAMACHY and OMI) observations. *J. Geophys. Res. Atmos.* **2011**, *116*, 1–13. [[CrossRef](#)]
26. Coheur, P.-F.; Clarisse, L.; Turquety, S.; Hurtmans, D.; Clerbaux, C. IASI measurements of reactive trace species in biomass burning plumes. *Atmos. Chem. Phys.* **2009**, *9*, 5655–5667. [[CrossRef](#)]
27. Liu, L.; Zhang, X.; Xu, W.; Liu, X.; Li, Y.; Lu, X.; Zhang, Y.; Zhang, W. Temporal characteristics of atmospheric ammonia and nitrogen dioxide over China based on emission data, satellite observations and atmospheric transport modeling since 1980. *Atmos. Chem. Phys. Discuss.* **2017**, *2017*, 1–32. [[CrossRef](#)]
28. Hertel, O.; Skjøth, C.A.; Reis, S.; Bleeker, A.; Harrison, R.; Cape, J.N.; Fowler, D.; Skiba, U.; Simpson, D.; Jickells, T.; et al. Governing processes for reactive nitrogen compounds in the European atmosphere. *Biogeosciences* **2012**, *9*, 4921–4954. [[CrossRef](#)]
29. Liu, X.; Duan, L.; Mo, J.; Du, E.; Shen, J.; Lu, X.; Zhang, Y.; Zhou, X.; He, C.; Zhang, F. Nitrogen deposition and its ecological impact in China: An overview. *Environ. Pollut.* **2011**, *159*, 2251–2264. [[CrossRef](#)] [[PubMed](#)]
30. Xu, W.; Luo, X.S.; Pan, Y.P.; Zhang, L.; Tang, A.H.; Shen, J.L.; Zhang, Y.; Li, K.H.; Wu, Q.H.; Yang, D.W.; et al. Quantifying atmospheric nitrogen deposition through a nationwide monitoring network across China. *Atmos. Chem. Phys.* **2015**, *15*, 12345–12360. [[CrossRef](#)]
31. Flechard, C.R.; Nemitz, E.; Smith, R.I.; Fowler, D.; Vermeulen, A.T.; Bleeker, A.; Erisman, J.W.; Simpson, D.; Zhang, L.; Tang, Y.S.; et al. Dry deposition of reactive nitrogen to European ecosystems: A comparison of inferential models across the NitroEurope network. *Atmos. Chem. Phys.* **2011**, *2011*, 2703–2728. [[CrossRef](#)]
32. Whitburn, S.; Van Damme, M.; Clarisse, L.; Bauduin, S.; Heald, C.L.; Hadji-Lazaro, J.; Hurtmans, D.; Zondlo, M.A.; Clerbaux, C.; Coheur, P.F. A flexible and robust neural network IASI-NH₃ retrieval algorithm. *J. Geophys. Res. Atmos.* **2016**, *121*, 6581–6599. [[CrossRef](#)]
33. Sahu, L.; Sheel, V.; Kajino, M.; Gunthe, S.S.; Thouret, V.; Nedelec, P.; Smit, H.G. Characteristics of tropospheric ozone variability over an urban site in Southeast Asia: A study based on MOZAIC and MOZART vertical profiles. *J. Geophys. Res. Atmos.* **2013**, *118*, 8729–8747. [[CrossRef](#)]
34. Xu, P.; Liao, Y.J.; Lin, Y.H.; Zhao, C.X.; Yan, C.H.; Cao, M.N.; Wang, G.S.; Luan, S.J. High-resolution inventory of ammonia emissions from agricultural fertilizer in China from 1978 to 2008. *Atmos. Chem. Phys.* **2016**, *16*, 1207–1218. [[CrossRef](#)]
35. Huang, X.; Song, Y.; Li, M.; Li, J.; Huo, Q.; Cai, X.; Zhu, T.; Hu, M.; Zhang, H. A high resolution ammonia emission inventory in China. *Glob. Biogeochem. Cycles* **2012**, *26*, 1–14. [[CrossRef](#)]
36. Kang, Y.; Liu, M.; Song, Y.; Huang, X.; Yao, H.; Cai, X.; Zhang, H.; Kang, L.; Liu, X.; Yan, X.; et al. High-resolution ammonia emissions inventories in China from 1980 to 2012. *Atmos. Chem. Phys.* **2016**, *16*, 2043–2058. [[CrossRef](#)]
37. Xu, P.; Zhang, Y.; Gong, W.; Hou, X.; Kroeze, C.; Gao, W.; Luan, S. An inventory of the emission of ammonia from agricultural fertilizer application in China for 2010 and its high-resolution spatial distribution. *Atmos. Environ.* **2015**, *115*, 141–148. [[CrossRef](#)]
38. Zhang, Y.; Dore, A.; Ma, L.; Liu, X.; Ma, W.; Cape, J.; Zhang, F. Agricultural ammonia emissions inventory and spatial distribution in the North China Plain. *Environ. Pollut.* **2010**, *158*, 490–501. [[CrossRef](#)] [[PubMed](#)]
39. Aneja, V.P.; Chauhan, J.; Walker, J. Characterization of atmospheric ammonia emissions from swine waste storage and treatment lagoons. *J. Geophys. Res. Atmos.* **2000**, *105*, 11535–11545. [[CrossRef](#)]

40. Pan, Y.; Wang, Y.; Tang, G.; Wu, D. Spatial distribution and temporal variations of atmospheric sulfur deposition in Northern China: Insights into the potential acidification risks. *Atmos. Chem. Phys.* **2013**, *13*, 1675–1688. [[CrossRef](#)]
41. Fuente, A.D.L.; Bing, N.; Hoeschele, I.; Mendes, P. Discovery of meaningful associations in genomic data using partial correlation coefficients. *Bioinformatics* **2004**, *20*, 3565. [[CrossRef](#)] [[PubMed](#)]
42. Sommer, S.G.; Olesen, J.E.; Christensen, B.T. Effects of temperature, wind speed and air humidity on ammonia volatilization from surface applied cattle slurry. *J. Agric. Sci.* **1991**, *117*, 91–100. [[CrossRef](#)]
43. Cassity-Duffey, K.; Cabrera, M.; Rema, J. Ammonia Volatilization from Broiler Litter: Effect of Soil Water Content and Humidity. *Soil Sci. Soc. Am. J.* **2015**, *79*, 543–550. [[CrossRef](#)]
44. Vet, R.; Artz, R.S.; Carou, S.; Shaw, M.; Ro, C.-U.; Aas, W.; Baker, A.; Bowersox, V.C.; Dentener, F.; Galy-Lacaux, C.; et al. A global assessment of precipitation chemistry and deposition of sulfur, nitrogen, sea salt, base cations, organic acids, acidity and pH, and phosphorus. *Atmos. Environ.* **2014**, *93*, 3–100. [[CrossRef](#)]
45. Zhao, Y.; Zhang, L.; Chen, Y.; Liu, X.; Xu, W.; Pan, Y.; Duan, L. Atmospheric nitrogen deposition to China: A model analysis on nitrogen budget and critical load exceedance. *Atmos. Environ.* **2017**, *153*, 32–40. [[CrossRef](#)]
46. Dong, W.X.; Xing, J.; Wang, S.X. Temporal and spatial distribution of anthropogenic ammonia emissions in China: 1994–2006. *Huanjing Kexue Environ. Sci.* **2010**, *31*, 1457–1463.
47. Zhang, L.; Jacob, D.J.; Knipping, E.M.; Kumar, N.; Munger, J.W.; Carouge, C.; Van Donkelaar, A.; Wang, Y.; Chen, D. Nitrogen deposition to the United States: Distribution, sources, and processes. *Atmos. Chem. Phys.* **2012**, *12*, 4539–4554. [[CrossRef](#)]



© 2017 by the authors. Licensee MDPI, Basel, Switzerland. This article is an open access article distributed under the terms and conditions of the Creative Commons Attribution (CC BY) license (<http://creativecommons.org/licenses/by/4.0/>).